Understanding the perovskite/self-assembled selective contact interface for ultra-stable and highly efficient p–i–n perovskite solar cells

Article *in* Energy & Environmental Science · May 2021

DOI: 10.1039/d0ee03807e

CITATIONS
65

READS
1,132

11 authors, including:

Ece Aktas
University of Naples Federico II
25 PUBLICATIONS **313** CITATIONS
SEE PROFILE

Nga Phung
Eindhoven University of Technology
34 PUBLICATIONS **2,289** CITATIONS
SEE PROFILE

Hans Köbler
Helmholtz-Zentrum Berlin
33 PUBLICATIONS **1,438** CITATIONS
SEE PROFILE

Dora Alejandra Gonzalez Ruiz
ICIQ Institute of Chemical Research of Catalonia
5 PUBLICATIONS **67** CITATIONS
SEE PROFILE

Energy & Environmental Science

ROYAL SOCIETY OF CHEMISTRY

PAPER

View Article Online
View Journal

Cite this: DOI: 10.1039/d0ee03807e

Understanding the perovskite/self-assembled selective contact interface for ultra-stable and highly efficient p–i–n perovskite solar cells†

Ece Aktas, ‡[ab] Nga Phung, ‡§[c] Hans Köbler, [c] Dora A. González, [ad] Maria Méndez, [a] Ivona Kafedjiska, [e] Silver-Hamill Turren-Cruz, [c] Robert Wenisch, [e] Iver Lauermann, [e] Antonio Abate *[cf] and Emilio Palomares *[ag]

Received 3rd December 2020,
Accepted 27th April 2021

DOI: 10.1039/d0ee03807e

rsc.li/ees

Current perovskite solar cell efficiency is close to silicon's record values. Yet, the roadblock for industrialization of this technology is its stability. The stability of the solar cell not only depends on the stability of the perovskite material itself but also notably on its contact layers and their interface with the perovskite, which plays a paramount role. This study rationalizes the design of new molecules to form self-assembled monolayers as a hole-selective contact. The new molecules increased the stability of the perovskite solar cells to maintain 80% of their initial PCE of 21% for 250 h at 85 °C under 1 sun illumination. The excellent charge collection properties as well as perovskite passivation effect enable the highly stable and efficient devices to demonstrate the vast potential of this new type of contact in photovoltaic application.

Broader context

Perovskite solar cells (PSCs) have rapidly become one of the hot topics in photovoltaics due to their high solar to energy conversion efficiency. The fast development of device engineering has allowed the preparation of solar cells with power conversion efficiency (PCE) over 25% within ten years. A perovskite layer is typically sandwiched between an electron selective layer and a hole selective layer to achieve high PCE and long-term stable PSCs. In standard PSCs, the charge selective layer plays a major role and the use of a self-assembled monolayer (SAM) as a charge selective layer has been lately explored due to its excellent charge selective properties. However, the design of the SAM is critical for achieving reproducible, high efficient, and ultra-stable perovskite devices. Herein, we have demonstrated the importance of molecule design on device performance and long-term stability. In particular, we have demonstrated that the use of SAMs results in a higher stability of the device compared to that with a pragmatic polymer selective contact. Our work will unveil a possibility for further promoting the performance and stability of PSCs and provide a valuable additional study to design charge selective contacts for PSCs.

Introduction

In a short span of 10 years of research, the efficiency of perovskite solar cells (PSCs) has reached over 25% from an initial 3.8%.[1] All through this process, the past knowledge in dye-sensitized solar cells and organic solar cells has been vital in achieving the rapid success. Moreover, charge selective contact layers are critical for achieving such high efficiency. Yet, despite having extraordinary progress in the device efficiency, the lack of long-term stability of halide perovskites is one of the main roadblocks towards its industrialization. To improve the device's stability, not only the intrinsic stability enhancement of halide perovskite is essential, but the stability of the device contact layers also plays a crucial role. Highly-priced organic charge selective materials drive the research to look for new organic conjugated molecules like self-assembled

[a] Institute of Chemical Research of Catalonia (ICIQ-BIST), Avda. Països Catalans, 16, Tarragona E-43007, Spain. E-mail: epalomares@ICIQ.es
[b] Departament de Química-Física i Inorgànica, URV, E-43007, Spain
[c] Helmholtz-Zentrum Berlin für Materialien und Energie GmbH, Kekuléstr. 5, Berlin D-12489, Germany. E-mail: antonio.abate@helmholtz-berlin.de, antonio.abate@unina.it
[d] Departament d'Enginyeria Electrònica, Elèctrica i Automàtica. URV, Tarragona E-43007, Spain
[e] PVcomB/Helmholtz-Zentrum Berlin für Materialien und Energie GmbH, Schwarzschildstraße 3, 12489 Berlin, Germany
[f] Department of Chemical, Materials and Production Engineering, University of Naples Federico II, Piazzale Tecchio 80, 80125 Fuorigrotta, Italy
[g] ICREA, Passeig LLuís Companys 23, E-08010, Spain

† Electronic supplementary information (ESI) available. See DOI: 10.1039/d0ee03807e

‡ Contributed equally to this work.

§ Present address: Department of Applied Physics, Eindhoven University of Technology, 5600 MB Eindhoven, the Netherlands.

monolayers (SAMs), which have been applied before in organic-based optoelectronic devices. Recently, SAMs have been used as the charge selective contacts for PSCs and the record power conversion efficiency has rapidly achieved 21% under standard measurement conditions.[2–4]

Unlike the organic hole selective materials that are expensive (*e.g.* PTAA costs 1000 euros per gram) or unstable in devices,[5] SAMs offer an opportunity for a cheap, scalable, and stable hole-selective material in the p–i–n type PSC structure due to their low material consumption, simple processing, and modifiable bandgap, without the requirement of dopants. In addition to these advantages, SAMs can modulate the work function of the metal oxide surface for better control of the energy band alignment between the different materials and interfaces within the solar cell. This modulation can be achieved *via* SAMs' anchoring groups such as carboxylic acid or phosphonic acid that can react with the surface hydroxyl groups of metal oxides *via* a simple chemical reaction.[6,7] Their functional groups are designed to modify the interface or surface properties like wetting, functionalities and, as mentioned above, the interfacial energy level alignment.[8–10] The linkage group is positioned between the anchoring group and the functional group, which determines the packing geometries.

In this study, we designed and synthesized two new carbazole based self-assembled molecules for hole-selective layers (HSLs) in p–i–n solar cells. We demonstrate stable efficiency above 21% delivering a solar cell open-circuit voltage (V_{OC}) of 1.19 V for a perovskite bandgap of 1.63 eV using these two SAMs. Remarkably, the solar cells retain 80% of their initial conversion efficiency after 250 h of maximum power point tracking under one sun AM 1.5 G illumination at 85 °C. These results are a new milestone for the development of a new class of hole selective materials for PSCs, which exhibit at the same time high efficiency and stability, which are paramount for the necessary transfer to industrial applications.

Result and discussion

Molecule design and characterization

Fig. 1a shows the synthesis pathway of the new SAMs, where 4-(3,6-bis(2,4-dimethoxyphenyl)-9*H*-carbazol-9-yl)benzoic acid (EADR03) and 4′-(3,6-bis(2,4-dimethoxyphenyl)-9*H*-carbazol-9-yl)-[1,1′-biphenyl]-4-carboxylic acid (EADR04) have a carbazole moiety as an electron donor unit.[11] On the one hand, the carbazole chemical group has electron-rich block properties, which lead to increase in power conversion efficiencies (PCE) up to 18% in PSCs.[12–14] Subsequent electron-rich groups are mainly added as substituents in the carbazole moiety to align the energy levels with the perovskite material and increase its solubility in common organic solvents. On the other hand, the substituted position of the photo-active conjugated phenyl benzene plays a critical role in the electron-donating effect. For instance, if the methoxy groups are only located at the *meta*-position, they will have an electron-withdrawing effect.[15] Nevertheless, if they is only positioned at the *ortho*-position, they will twist the phenyl ring out of the plane, causing the undesired steric effect.[16] For these reasons, 1,3-dimethoxybenzene is chosen as a substituent for the carbazole moiety. The synthetic details are given in the ESI.†

To prove its suitable energetic properties as a hole selective material for PSCs, we performed ultra-violet photoelectron spectroscopy (UPS) on the SAM layer attached to the indium-tin-oxide (ITO) substrate, similar to what is used in the device. The condensation reaction occurs between the carboxylic acid (–COOH) anchoring group of SAMs and the surface hydroxyl group (–OH) of metal oxide to give ester (O–C═O) type linkages,[6,17] which result in the formation of SAM on the ITO. The optical bandgap of SAMs is estimated from the absorption edge wavelength ($\lambda_{a.e.}$) using UV-vis measurement[18] (see Fig. S3 and Table S2, ESI†). From UPS measurement and optical bandgap, we calculate the position of the SAM's lowest unoccupied molecular orbital (LUMO). The valence band onset and the Fermi level value EADR03 and EADR04 are schematically displayed in Fig. 1b. In this study, we employed the triple cation perovskite ($Cs_{0.05}FA_{0.79}MA_{0.16}Pb(I_{0.84}Br_{0.16})_3$ hereafter labelled as CsFAMA) as the absorber layer adapted from Saliba *et al.*[19] The energetic properties of PTAA and CsFAMA are obtained from the literature and all values are referenced to the vacuum level.[3] As can be seen from Fig. 1b, SAMs exhibit a better electron blocking character than PTAA due to the carbazole unit in small molecule backbone, while working as efficient hole extraction layers.

Additionally, as shown in Fig. 1a, we designed the SAM molecules with the 1,3-dimethoxybenzene moiety acting as the terminal group that provides a miscible interface for the perovskite one-step solution process. A miscible interface ensures a homogenous and compact perovskite film.[20] To determine the surface wettability, contact angle measurements are performed on bare ITO and p-type materials deposited on ITO (see the Method section for details). The contacting angles of the water on bare ITO, PTAA, EADR03 and EADR04 are 8.13°, 88.15°, 50.19° and 51.63°, respectively (see Fig. S4, ESI†). The PTAA layer shows a higher hydrophobicity than the SAMs in agreement with the previous report,[21] leading to a poor wetting for perovskite solution on PTAA. We note that in the XRD patterns (see Fig. S9, ESI†), although there is no detectable peak shift or peak broadening in the perovskite phase, there is a noticeable more pronounced PbI_2 phase in the perovskite on PTAA than on SAMs. This higher PbI_2 content is also visible in the SEM images as a bright small grain on the surface (see Fig. S10, ESI†). Although it has been reported that excess PbI_2 in the perovskite can improve the device performance,[22] a recent report has shown that perovskite with a higher PbI_2 content can lead to a lower stability in devices due to the formation of metallic Pb, which can act as a non-radiative recombination center,[23] which will be discussed in details in the later section.

We examined the atomic bonds of SAMs on metal oxide surface using X-ray photoelectron spectroscopy (XPS). The spectra were analyzed as described in the ESI† (see Table S3). The C1s spectra, were decomposed into 4 peaks assigned to

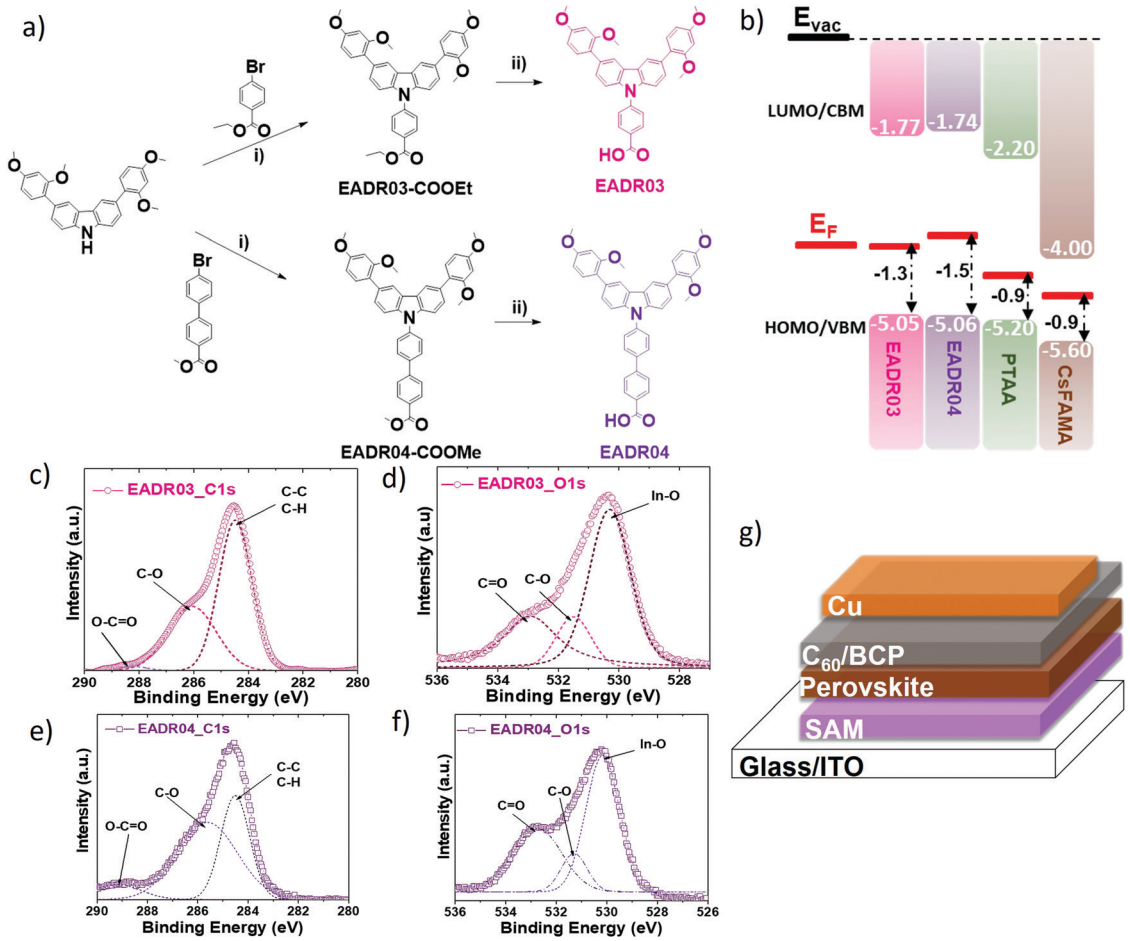

Fig. 1 (a) Synthesis pathway of SAMs; (i) tris(dibenzylideneacetone)dipalladium(0) (0.10 equiv.), tri-*tert*-butylphosphine tetrafluoroborate (0.20 equiv.), sodium *tert*-butoxide (1.1 equiv.), dry toluene (10.0 mL), argon, 115 °C, and 24 h (ii) potassium hydroxide (10 equiv.), solvent mixture of methanol : tetrahydrofuran (1 : 1, v : v), 85 °C, and 24 h. (b) Energy alignment of different layers. The band edge positions of SAMs, PTAA and CsFAMA layers from UPS measurements in the schematic representation. Note that the SAM layer's values (EADR03 and EADR04) are measured using UPS (Fig. S8, ESI† shows UPS spectra) (see Methods for detail). Before UPS measurements, the ITO substrate was treated with UV-ozone to ensure similarity with the used substrates in devices. The XPS high-resolution survey spectra of (c) C1s and (d) O1s of ITO/EADR03 and (e) C1s and (f) O1s of ITO/EADR04. (g) Schematic representation of the used p–i–n device structure.

C–C or C–H at 284.6 eV (284.7 eV), C–O at 286.0 eV (285.9 eV), COOCH bonds at 287.0 eV (287.0 eV), and O–C=O bonds at 288.5 eV (289.1 eV) for EADR03 (EADR04) (Fig. 1c and e respectively).[24,25] The [C–O]/[C–C + C–O] area ratios amount to 25% for EADR03 and 30% for EADR04. From their structural formulae, one would expect 15% for EADR03 and 12% for EADR04 ignoring attenuation due to inelastic electron scattering. The evident excess in C–O bonds is likely caused by solvent residues. It is worth noting that the bare ITO surface also exhibits C1s peaks situated at 284.9 eV, 285.8 eV, 287.0 eV, and 289.1 eV (see Fig. S5a, ESI†). These carbon contributions are presumably largely residues from the cleaning procedure. The O1s region (Fig. 1d and f) exhibit peaks belonging to In–O at 530.1 eV, surface hydroxides at 530.9 eV (530.8 eV), C=O at 532.8 eV (532.8 eV) and C–O at 533.1 eV (533.2 eV) for EADR03 (EADR04) in the spectra.[26,27] The bare ITO substrate also showed four components: 530.3 eV (InSnO), 530.8 eV, 531.8 eV, and 532.9 eV (see Fig. S5b, ESI†), where the carbon compounds are again presumably cleaning residues.

The formation of ester bonds demonstrates bonding between the carbon atom of carboxylic acid and the oxygen atom of the hydroxyl group on ITO or to solvent residues.[28] Moreover, we observe a much weaker signal of this characteristic ester bond in C1s and O1s spectra of bare ITO in these regions, which further points to the presence of SAMs on ITO (see Fig. S6, ESI†). The N1s spectra show the same peak position of *ca.* 400 eV for both SAMs, indicating the presence of the C–N bond in the structure (see Fig. S6c, ESI†). These strongly indicate the presence of SAMs on the ITO substrate.

To understand the charge transfer properties of these new SAMs as HSLs for PSCs, we performed time-resolved photoluminescence (TRPL) using λ = 470 nm as the excitation wavelength as shown in Fig. S11 (ESI†). The traces exhibit two different decay profiles fitted to a bi-exponential function as previously reported.[29–31] SAM-based perovskite films show an initial fast decay that can be assigned to trap filling, while the slower decay most likely corresponds to the bimolecular recombination. The lifetimes τ_1 of EADR03, EADR04, PTAA

and the perovskite are 15 ns, 9 ns, 2 ns and 7 ns, respectively, and the calculated lifetimes τ_2 are 158 ns, 106 ns, 12 ns and 83 ns for EADR03, EADR04, PTAA and the perovskite, respectively (see Table S4, ESI†). Interestingly, in Fig. S11b (ESI†), the luminescence decay of the perovskite layers on SAMs shows efficient quenching that supports their efficient hole transporting character compared to PTAA. Not only is there evidence of a faster charge extraction using SAM compared to PTAA, but the increased PL yield can also indicate an interfacial passivation effect[32] compared to the PTAA sample shown in Fig. S11c (ESI†) similar to the reported carbazole based polymer.[33]

Photovoltaic performance

We employed in this study the state-of-the-art device architecture with ITO/SAM or PTAA/CsFAMA/C_{60}/BCP/Cu sandwich architecture as shown in Fig. 1g.[34] Cesium-containing triple cation perovskite (CsFAMA) is deposited on top of the HSLs using the one-step method. Afterwards, C_{60}, an electron selective layer, is thermally evaporated on top of the perovskite layer. The fullerene C_{60} has excellent electron-extraction properties in photovoltaic devices. Thus, it is preferred as the electron transport layer.[35] Lastly, a bathocuproine (BCP) buffer layer and copper (Cu) electrode are evaporated to complete the device. SAMs are generally deposited on metal oxide surfaces as a monolayer using a variety of methods like solution assisted self-assembly (dipping), vapour deposition and spin-coating method.[27] Here, we used the paradigmatic PTAA as our baseline to determine the performance of cells with SAMs. PTAA is widely used in the p–i–n PSCs as a polymeric HSL, which can be coated into a thin homogenous layer from solution and show PCEs higher than 18%.[5,36,37] The detailed fabrication process of the perovskite solar cells is presented in the Methods section of the ESI.†

The choice of solvent is the first critical step for SAMs to have a well-organized interface between SAMs and perovskite absorber. Here, the design of EADR03 and EADR04 consists of a carboxylic acid moiety on the molecule backbone, which makes the molecules soluble in non-halogenated solvents as ethanol (EtOH) and isopropanol (IPA). The devices with SAMs as HSLs show statistically better performance with IPA using the dipping method compared to ethanol (see Fig. S12 and S13, ESI†). The best PV parameters of solvent optimization are summarized in Table S5 (ESI†). Consequently, we achieve more than 20% PCE using the dipping method with EADR03 as the HSL, whereas spin coating method only provides a maximum of 17% (see Fig. S14 and S15, ESI†). The best device parameters of EADR03 with different deposition methods are shown in Table S6 (ESI†). On the other hand, EADR04 is not suitable for spin-coating methods because of solubility problems. We note that here the dipping method is preferable due to lower solubility of the molecules in alcohol. Nonetheless, the solubility is not the only deciding factor for device performance. The molecules have excellent solubility in toluene, yet the devices using this solvent exhibit unsatisfactory performance (Table S5, ESI†). The reason behind the difference in behavior is beyond the scope of this study and will require further research.

Fig. 2b shows the current density *versus* voltage (*J–V*) scans of the best devices with PTAA, EADR03 and EADR04 measured at a scan rate of 100 mV s^{-1} from forward (V_{OC} to J_{SC}) to reverse bias. Maximum power point (MPP) tracks of the best devices are shown in Fig. 2b. MPP-tracked efficiencies are comparable with the respective *J–V* values, which is expected from the negligible hysteresis. A statistical distribution of the cell parameters is achieved from more than 15 devices for each HSL, shown in Fig. 2a, exhibiting systematically a higher performance of SAM based cells compared to PTAA. The best PCEs of EADR03 and EADR04 are 20.5% and 20.6% surpassing PTAA cells' best value of 18.9%. Remarkably, the V_{OC} values of SAM-based devices demonstrate more than 1.1 V and the fill factor (FF) values $>80\%$. The superior electron blocking of the SAM compared to that of PTAA is attributed to the higher V_{OC} and FF values of EADR03 and EADR04 compared to those of PTAA. Specifically, the voltage of SAM-based devices is approximately 150 mV higher than that of PTAA. This improvement in device performance is not directly correlated to the HOMO level of the material as PTAA has a deeper HOMO level compared to SAMs (Fig. 1b); instead, SAM as a material, which has both efficient charge transport and passivation effects, results in this improvement. We emphasize that we achieved this desirable property of a contact layer without the use of dopants, which has been shown to degrade the perovskite layer.[38] Our result resonates with the conclusion of Al-Ashouri *et al.*[3] on phosphonic anchor SAMs. These results establish the tremendous promising benefit of SAM as an attractive class of selective layer materials realized in both perovskite and organic PV.[2,39,40]

In addition, the *J–V* scan of the SAM-HSL based full device showed a lower leakage current in place of PTAA under dark conditions, shown in Fig. S18 (ESI†). The low dark current also indicates a high density of SAM on ITO. The integrated J_{SC} of the best devices from external quantum efficiency measurement (EQE) integration is shown in Fig. 2c. The higher current density is also due to the lower parasitic absorption of SAM compared to that of PTAA in the short wavelength range similar to phosphonic SAMs developed for the same device architecture.[41] Integrated J_{SC} values have a negligible difference ($\sim$1 mA cm^{-2}) with the J_{SC} values gained from the *J–V* scans for the best device. The devices with the SAMs as HSLs show minor hysteresis index (HI)[42,43] between reverse and forward *J–V* scans. All photovoltaic parameters of the best devices are provided in Table 1.

As we have demonstrated the good passivation effect of SAM on the interface between perovskite and the HSLs compared to that of the commonly used polymer PTAA, the other interface with the electron selective layer is equally important. It has been reported that the interfacial recombination at perovskite/C_{60} dominates the losses in voltage of this device architecture and it can be improved by using an ultrathin passivation layer of LiF ($\sim$1 nm).[34] In this study, we used the same approach to enhance further the final V_{OC} of the device, reaching 1.19 V with 1.63 eV bandgap perovskite in EADR03 based cells. Table 1 summarizes the champion devices in this study. As shown in Table 1, the improvement brought by LiF is higher in SAM-based devices compared to that in PTAA-based ones. This can

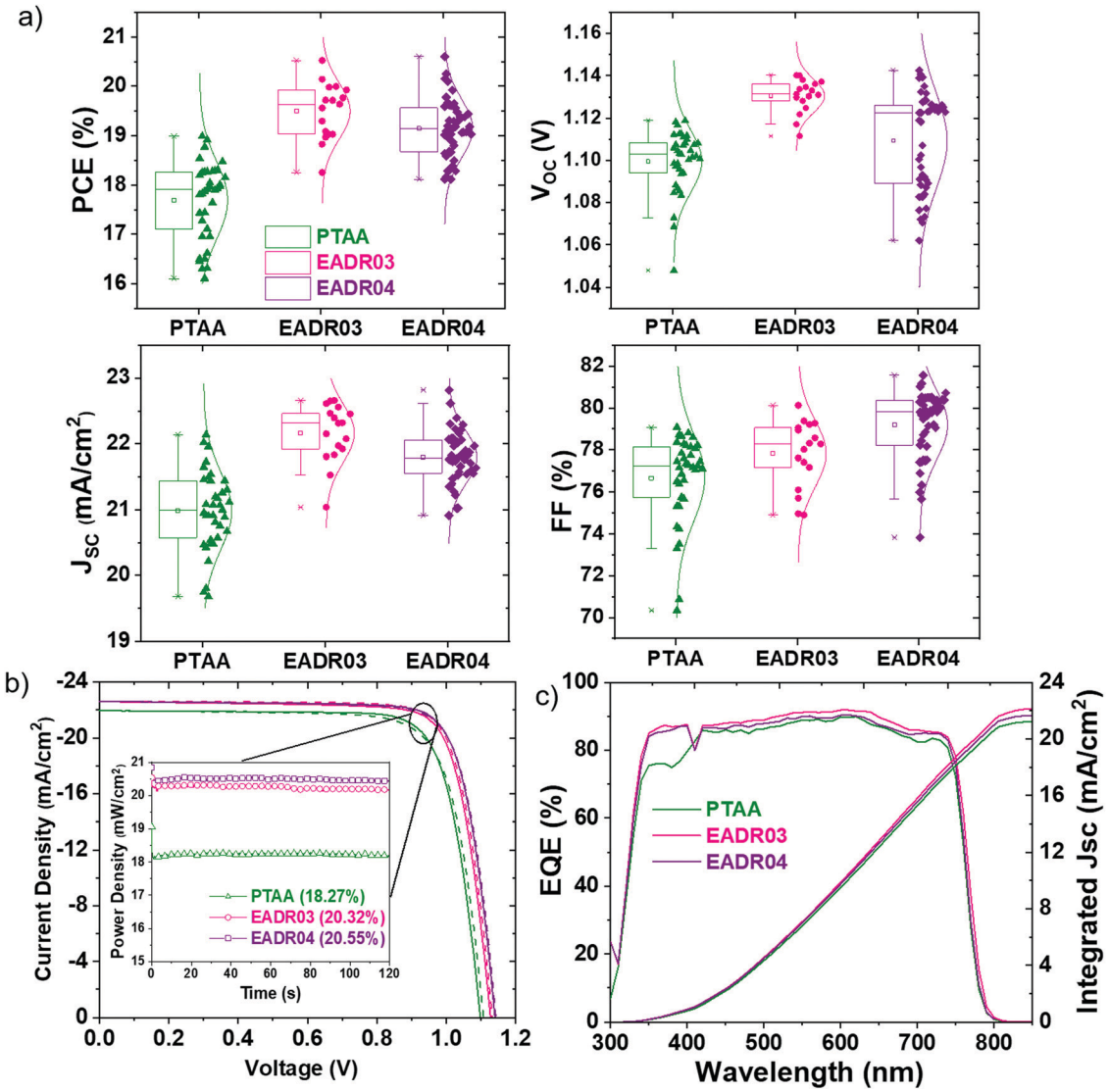

Fig. 2 (a) Device performance statistics with different hole selective layers. (b) Best *J*–*V* curves from PTAA, EADR03 and EADR04 with quasi-steady state efficiency. (c) Corresponding external quantum efficiency curves which show integrated current density in agreement with values from the *J*–*V* measurement.

be attributed to slightly higher PbI_2 content on the surface of the perovskite grown on PTAA than SAM (shown as a bright grain in the SEM images – Fig. S10, ESI†). The presence of PbI_2 on the surface can partially reduce the interfacial recombination at perovskite/C_{60} because of its wide bandgap.[44] With the improvement from LiF (the V_{OC} increases for more than 50 mV) and an anti-reflection coating, the SAM-based devices reache more than quasi-steady-state 21% for EADR03 and 20.7% for EADR04 after 2 minutes of MPP tracking (Fig. 3).

Table 1 Photovoltaic parameters of the best performing devices based on different HSLs with and without LiF and anti-reflection coating with a scan speed of 100 mV s^{-1}

HSLs	LiF	ARC	Integrated J_{SC} (mA cm^{-2})	J_{SC} (mA cm^{-2})	V_{OC} (mV)	FF (%)	PCE (%)	HI (%)
PTAA	No	No	21.2	21.9	1098	79	18.9	−0.01
PTAA	Yes	No	21.0	21.4	1124	78	18.8	0.06
PTAA	Yes	Yes	21.7	22.0	1105	78	18.9	0.00
EADR03	No	No	22.1	22.6	1132	80	20.5	0.00
EADR03	Yes	No	21.2	21.9	1186	79	20.5	0.03
EADR03	Yes	Yes	21.9	22.9	1156	80	21.2	0.00
EADR04	No	No	21.6	22.6	1140	80	20.6	−0.01
EADR04	Yes	No	21.0	22.2	1177	80	20.9	0.03
EADR04	Yes	Yes	21.8	22.6	1164	80	21.0	0.00

Device stability investigation

Perovskite-based PVs have reached 25.5% certified PCE and surpassed the conventional PV thin-film technologies and are approaching the state-of-the-art silicon single-junction solar cell.[45] However, the main problem for the integration of perovskite into the PV industry is its lack of stability.[46] Here, we use a high through-put ageing setup, which can track hundreds of devices at once. We compared the stability of

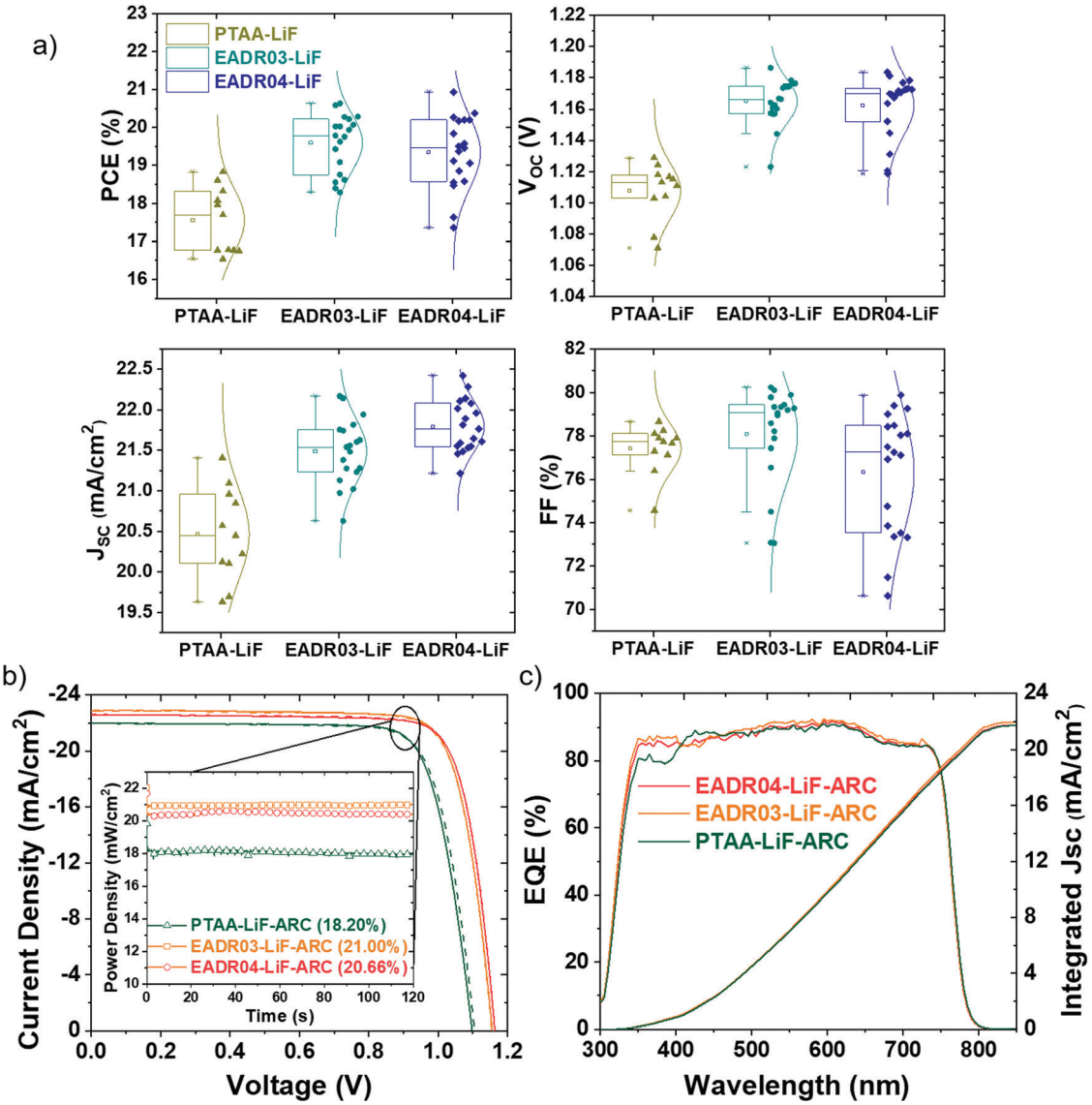

Fig. 3 (a) Device performance statistics of a total of 50 devices from PTAA, EADR03 and EADR04 with LiF. (b) Best *J*–*V* curves from PTAA, EADR03 and EADR04 with LiF and anti-reflection coating in the devices with quasi-steady state efficiency. (c) Corresponding external quantum efficiency curves which show integrated current density in agreement with values from the *J*–*V* measurement with anti-reflection coating.

PTAA with that of EADR03 and EADR04 cells in the continuous MPP in one sun illumination. As can be seen in Fig. 4a, the PTAA cells rapidly lost more than 15% of their initial PCE after 24 hours of MPP tracking, on the other hand, the SAM based devices exhibit excellent higher stability (note that the curves are averaged from different devices and show statistical values rather than only that of the best device).

Although the EADR04 cells show a fast drop in the first few hours, they regain their initial efficiency and retain 95% of the initial efficiency after 150 h of continuous MPP tracking before they have a declining trend. We extrapolate this trend and estimate that the T_{80} (time until the cell reaches 80% of its initial efficiency) can be more than 800 hours for EADR04 cells. Compared to the EADR04 cells, the EADR03 cells gradually decrease until they reach 80% of their initial PCE at around 180 h (as can also be seen in Table 2). This trend is more evident when the EADR04 cells are aged at an elevated temperature of 85 °C (see Fig. 4b) where the cells retain 80% of their initial efficiency for approximately 250 h of continuous MPP tracking. This difference between the two SAMs can be attributed to the structure of the molecules. As can be seen in Fig. S1 (ESI†), EADR04 has higher decomposition temperature compared to EADR03, thanks to the extra phenyl in the linkage group (chain), between the anchoring group and the functional group. Note that the thermogravimetry indicates the decomposition temperatures (180 °C for EADR03 and 354 °C for EADR04), which are indeed not the same temperature as the operational conditions. However, thermogravimetry can still indicate the resiliency of the molecules at high temperature and under long-time operation conditions. Similar to our observation, Li *et al.* have reported that different conjugated side-chain polymers result in devices with a higher thermal stability.[47]

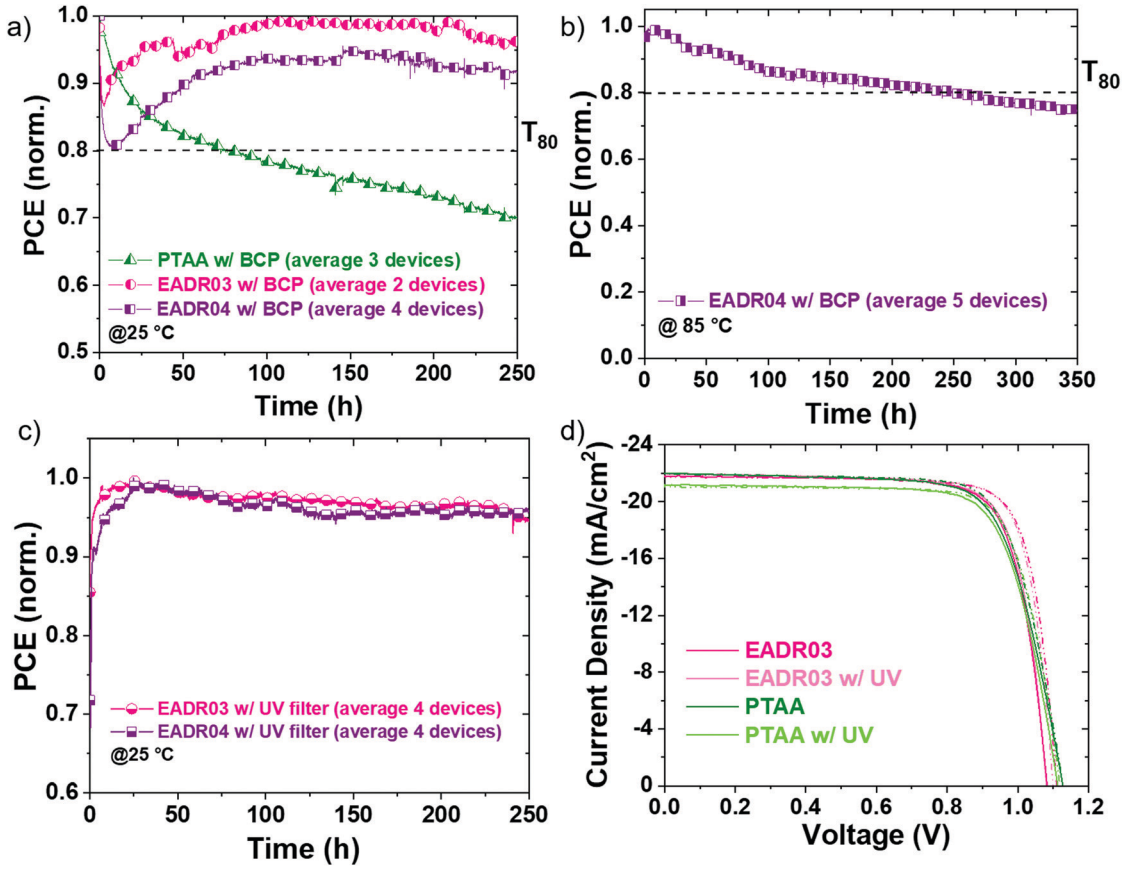

Fig. 4 Long-term continuous maximum power point tracking of (a) EADR03, EADR04 and PTAA based devices with BCP at 25 degrees Celsius. (b) EADR04 with BCP at 85 degrees Celsius. (c) EADR03 and EADR04 based devices with a UV filter (cut-off at 350 nm) at 25 degrees Celsius. Note that the values were averaged from different devices from different batches. All the measurements were done in an N_2 atmosphere without encapsulation. (d) Best J–V curves from PTAA and EADR03 with and without UV light exposure (365 nm) for 30 minutes, prior to perovskite layer fabrication.

Table 2 Estimated T_{80} of the p–i–n perovskite solar cell with different HSLs from the MPP traces with and without a UV filter

HSLs	Initial PCE (%)	Ageing temperature and illumination	Tracking time (h)	Estimated T_{80} (h)
PTAA	18.5	25 °C, metal-halide lamp, 100 mW cm^{-2}	250	81
EADR03	19.3	25 °C, metal-halide lamp, 100 mW cm^{-2}	250	183
EADR03	19.9	25 °C, metal-halide lamp with UV filter, 100 mW cm^{-2}	250	1574
EADR04	17.9	25 °C, metal-halide lamp, 100 mW cm^{-2}	250	872
EADR04	19.9	25 °C, metal-halide lamp with UV filter, 100 mW cm^{-2}	250	2086
EADR04	20.1	85 °C, metal-halide lamp, 100 mW cm^{-2}	250	242
PTAA[a]	16	25 °C, White LED, 100 mW cm^{-2}	170	9000

[a] The selected report has a similar device architecture under inert gas conditions and room temperature.[37]

We attribute this encouraging improvement in the stability of SAMs as HSLs compared to PTAA to the excellent stability of SAMs in UV light. Indeed, when we expose PTAA layers to the UV light for 30 minutes prior to perovskite deposition, the device exhibits lower J_{SC} whereas UV light has negligible effect on EADR03 (as can be seen in Fig. 4d). This negative impact on device performance is more evidenced in the device statistics shown in Fig. S19 (ESI†) where PTAA cells lose on average more than 1 mA cm^{-2} after UV exposure. We emphasize that even without any UV light stress on the perovskite absorber layer, the UV light has a detrimental effect on PTAA in contrast to the SAMs whose devices did not show this behaviour.

The UV-induced degradation in PTAA is very likely due to the breaking of the carbon bonds in the aromatic rings into smaller fragments.[48] In addition, polymers have been reported to undergo the photochemical pathway in which the polymer hydrocarbon chain can break down into free radicals in the presence of oxygen. This UV-photochemical reaction can severely deteriorate the polymeric material properties.[49] This also indicates a potential degradation pathway of the polymer HSLs in ambient air that is undesirable for PSC application.

We acknowledge that a bulk of PTAA (~10 nm) and a single molecular layer (1–3 nm) might not be directly comparable in this study. The UV absorption of the SAM layer is negligible compared to that of the PTTA layer. We do expect that the absorption of PTAA layer is about 1 order of magnitude higher than that of the SAM layer if we only consider the thicknesses of the two layers. Therefore, the defects that the UV absorption may create are more likely to impact the PTAA layer than the SAM layer. However, achieving an even thinner PTAA with a comparable thickness with the SAM layers poses practical challenges. In fact, Stolterfoht *et al.* demonstrated that diluting PTAA solution led to having an incomplete coverage of ITO, decreasing the selectivity of the PTAA layer under the perovskite layer, which negatively affected device's FF and V_{OC}.[50]

In this work, we have significantly higher intensity in the range of 300–500 nm with the lamp used for ageing measurements compared to global AM1.5 spectrum (see Fig. S20a, ESI†). Hence, the measurement condition accelerates the UV-induced PTAA degradation, which can be the reason behind the lower stability of our PTAA p–i–n cells compared to the values reported in the literature (shown in Table 2). We note that high stability of PTAA in n–i–p cells has been reported;[51] nonetheless, in the n–i–p structure, the UV photons are absorbed in the n-type and perovskite absorber layers before reaching PTAA. Moreover, this is also an accelerating ageing measurement for perovskite. The instability of perovskite under UV light has been widely reported,[52,53] mainly because of the photochemical degradation of PbI_2 into metallic lead Pb^0 forming non-radiative recombination centers, reducing the cells' efficiency.[23] We used a UV filter (cut-off at 350 nm) to improve the lifetime of the devices (see Fig. 4c). Although we still have a significantly higher intensity of the simulated spectrum in the 350–500 nm region compared to global AM1.5 (see Fig. S21b, ESI†), we do see a considerable enhancement of the cells' lifetimes as can be seen in Table 2 (we note that the light intensity is lower than one sun illumination). With the UV-filter, the EADR04 cells' T_{80} reaches a value of more than 2000 h. Therefore, the reported values in Table 2 are an underestimation of the cells' potential in this study.

Conclusion

This study demonstrates the importance of the molecular design when using SAMs as the selective contacts in perovskite solar cells. The SAMs have become the route to achieve high solar-to-energy conversion efficiencies and, herein, we show that SAMs can lead to remarkably stable solar cells. In our study, we use both the carbazole and methoxy moieties as electron donors for efficient charge selection, good electron blocking properties and surface passivation of the perovskite. Moreover, the 1,3-dimethoxybenzene terminal group of the molecule is compatible with perovskite formation resulting in a smooth and compact perovskite film. This design enables the perovskite cells to reach more than 21% stabilized efficiency and, most importantly, the monolayer based devices exhibit superior stability compared to PTAA based cells, which are the current standard for perovskite solar cells approaching silicon PV values. We demonstrated that stabilizing the perovskite/SAMs interface is the way to commercialize perovskite solar cells.

Author contributions

EA and NP conceived the idea, formulated the project and wrote the first draft of the manuscript under the supervision of EP and AA. EA and DR synthesized EADR03 and EADR04. EA and NP fabricated the devices and carried out the photo-physical characterization. HK and SHT carried out the Maximum Power Point Tracking studies of the devices. MM carried out Time-Correlated Single Photon Counting Measurements. RW and IK carried out X-ray Photoelectron Spectroscopy and Ultra-violet Photoelectron measurements under the supervision of IL. All authors participated in the discussion of the results and the manuscript writing and, finally, approved the submission.

Conflicts of interest

There are no conflicts to declare.

Acknowledgements

EA, DR, MM, and EP thank MINECO (projects CTQ2013-47183, CTQ2017-89814-P, and CTQ2017-85393-P) and SGR-AGAUR 2017SGR00978. EP is also thankful to ICIQ and ICREA for financial support. This result is part of a project that has received funding from the European Research Council (ERC) under the European Union's Horizon 2020 research and innovation programme grant agreement No. number 804519. IK, IL, and RW acknowledge financial support by the German Federal Ministry for Economic Affairs and Energy in the frame of the speedCIGS project number 0324095D. EA thanks ICIQ for funding the internship in HZB. The authors thank Carola Klimm for taking SEM microscopic images. EA thanks Dr Natalia Maticiuc for supporting XPS and UPS data analysis. NP thanks Amran Al-Ashouri for optimizing the device fabrication processes.

References

1 A. Kojima, K. Teshima, Y. Shirai and T. Miyasaka, Organometal Halide Perovskites as Visible- Light Sensitizers for Photovoltaic Cells, *J. Am. Chem. Soc.*, 2009, **131**, 6050–6051.
2 E. Yalcin, *et al.*, Semiconductor self-assembled monolayers as selective contacts for efficient PiN perovskite solar cells, *Energy Environ. Sci.*, 2019, **12**, 230–237.
3 A. Al-Ashouri, *et al.*, Conformal monolayer contacts with lossless interfaces for perovskite single junction and monolithic tandem solar cells, *Energy Environ. Sci.*, 2019, **12**, 3356–3369.
4 L. Li, *et al.*, Self-assembled naphthalimide derivatives as an efficient and low-cost electron extraction layer for

n-i-p perovskite solar cells, *Chem. Commun.*, 2019, **55**, 13239–13242.
5 T. Y. Yang, *et al.*, Achieving Long-Term Operational Stability of Perovskite Solar Cells with a Stabilized Efficiency Exceeding 20% after 1000 h, *Adv. Sci.*, 2019, **6**, 1–7.
6 B. J. Brennan, *et al.*, Comparison of silatrane, phosphonic acid, and carboxylic acid functional groups for attachment of porphyrin sensitizers to TiO2 in photoelectrochemical cells, *Phys. Chem. Chem. Phys.*, 2013, **15**, 16605–16614.
7 R. Qiao and L. Zuo, Self-assembly monolayers boosting organic-inorganic halide perovskite solar cell performance, *J. Mater. Res.*, 2018, **33**, 387–400.
8 J. C. Love, L. A. Estroff, J. K. Kriebel, R. G. Nuzzo and G. M. Whitesides, Self-Assembled Monolayers of Thiolates on Metals as a Form of Nanotechnology, *Chem. Rev.*, 2005, **105**, 1103–1170.
9 K. Wojciechowski, *et al.*, Heterojunction modification for highly efficient organic-inorganic perovskite solar cells, *ACS Nano*, 2014, **8**, 12701–12709.
10 S. Casalini, C. A. Bortolotti, F. Leonardi and F. Biscarini, Self-assembled monolayers in organic electronics, *Chem. Soc. Rev.*, 2017, **46**, 40–71.
11 X. Zhu, *et al.*, Hole-Transporting Materials Incorporating Carbazole into Spiro-Core for Highly Efficient Perovskite Solar Cells, *Adv. Funct. Mater.*, 2018, **29**, 1807094.
12 C. Lu, I. T. Choi, J. Kim and H. K. Kim, Simple synthesis and molecular engineering of low-cost and star-shaped carbazole-based hole transporting materials for highly efficient perovskite solar cells, *J. Mater. Chem. A*, 2017, **5**, 20263–20276.
13 X. Yin, *et al.*, One-step facile synthesis of a simple carbazole-cored hole transport material for high-performance perovskite solar cells, *Nano Energy*, 2017, **40**, 163–169.
14 C. Rodríguez-Seco, *et al.*, Minimization of Carrier Losses for Efficient Perovskite Solar Cells through Structural Modification of Triphenylamine Derivatives, *Angew. Chem., Int. Ed.*, 2020, **132**, 5341–5345.
15 N. J. Jeon, *et al.*, o-Methoxy Substituents in Spiro-OMeTAD for Efficient Inorganic–Organic Hybrid Perovskite Solar Cells, *J. Am. Chem. Soc.*, 2014, **136**, 7837–7840.
16 A. Krishna and A. C. Grimsdale, Hole transporting materials for mesoscopic perovskite solar cells – towards a rational design?, *J. Mater. Chem. A*, 2017, **5**, 16446–16466.
17 M. K. Nazeeruddin, R. Humphry-Baker, P. Liska and M. Grätzel, Investigation of Sensitizer Adsorption and the Influence of Protons on Current and Voltage of a Dye-Sensitized Nanocrystalline TiO_2 Solar Cell, *J. Phys. Chem. B*, 2003, **107**, 8981–8987.
18 J. C. S. Costa, R. J. S. Taveira, C. F. R. A. C. Lima, A. Mendes and L. M. N. B. F. Santos, Optical band gaps of organic semiconductor materials, *Opt. Mater.*, 2016, **58**, 51–60.
19 M. Saliba, *et al.*, Cesium-containing triple cation perovskite solar cells: Improved stability, reproducibility and high efficiency, *Energy Environ. Sci.*, 2016, **9**, 1989–1997.
20 L. Zuo, *et al.*, Enhanced Photovoltaic Performance of CH_3 NH_3PbI_3 Perovskite Solar Cells through Interfacial Engineering Using Self-Assembling Monolayer, *J. Am. Chem. Soc.*, 2015, **137**, 2674–2679.
21 Z. Safari, *et al.*, Optimizing the interface between hole transporting material and nanocomposite for highly efficient perovskite solar cells, *Nanomaterials*, 2019, **9**, 1627.
22 T. Du, *et al.*, Formation, location and beneficial role of PbI2 in lead halide perovskite solar cells, *Sustainable Energy Fuels*, 2017, **1**, 119–126.
23 B. Roose, K. Dey, Y.-H. Chiang, R. H. Friend and S. D. Stranks, A Critical Assessment of the Use of Excess Lead Iodide in Lead Halide Perovskite Solar Cells, *J. Phys. Chem. Lett.*, 2020, **11**, 6505–6512.
24 C. Tozlu, *et al.*, Effect of TiO2 modification with amino-based self-assembled monolayer on inverted organic solar cell, *Appl. Surf. Sci.*, 2017, **422**, 1129–1138.
25 J. F. Moulder, W. F. Stickle, P. E. Sobol and K. D. Bomben, *Handbook of X-ray Photoelectron Spectroscopy*, Chastain, Publ. by PerkinElmer Corp., 1992.
26 F. Montagne, J. Polesel-Maris, R. Pugin and H. Heinzelmann, Poly(N-isopropylacrylamide) thin films densely grafted onto gold surface: preparation, characterization, and dynamic AFM study of temperature-induced chain'conformational changes, *Langmuir*, 2009, **25**, 983–991.
27 C. Yan, M. Zharnikov, A. Gölzhäuser and M. Grunze, Preparation and characterization of self-assembled monolayers on indium tin oxide, *Langmuir*, 2000, **16**, 6208–6215.
28 E. Arkan, *et al.*, Effect of functional groups of self assembled monolayer molecules on the performance of inverted perovskite solar cell, *Mater. Chem. Phys.*, 2020, **254**, 123435.
29 E. J. Palomares, *et al.*, Supramolecular Coordination of Pb2+ Defects in Hybrid Lead Halide Perovskite Films Using Truxene Derivatives as Lewis Base Interlayers, *ChemPhysChem*, 2019, **20**, 2702–2711.
30 J. Kim, *et al.*, Excitation Density Dependent Photoluminescence Quenching and Charge Transfer Efficiencies in Hybrid Perovskite/Organic Semiconductor Bilayers, *Adv. Energy Mater.*, 2018, **1802474**, 1–11.
31 X. Wen, *et al.*, Defect trapping states and charge carrier recombination in organic-inorganic halide perovskites, *J. Mater. Chem. C*, 2015, **4**, 793–800.
32 E. M. Hutter, T. Kirchartz, B. Ehrler, D. Cahen and E. von Hauff, Pitfalls and prospects of optical spectroscopy to characterize perovskite-transport layer interfaces, *Appl. Phys. Lett.*, 2020, **116**, 100501.
33 W. Okada, T. Suga, K. Oyaizu, H. Segawa and H. Nishide, Perovskite/TiO_2 Interface Passivation Using Poly(vinylcarbazole) and Fullerene for the Photovoltaic Conversion Efficiency of 21%, *ACS Appl. Energy Mater*, 2019, **2**, 2848–2853.
34 M. Stolterfoht, *et al.*, Visualization and suppression of interfacial recombination for high-efficiency large-area pin perovskite solar cells, *Nat. Energy*, 2018, **3**, 847–854.
35 K. Wojciechowski, *et al.*, C60 as an Efficient n-Type Compact Layer in Perovskite Solar Cells, *J. Phys. Chem. Lett.*, 2015, **6**, 2399–2405.

36 M. Saliba, *et al.*, How to Make over 20% Efficient Perovskite Solar Cells in Regular (n–i–p) and Inverted (p–i–n) Architectures, *Chem. Mater.*, 2018, **30**, 4193–4201.
37 M. Stolterfoht, *et al.*, Approaching the fill factor Shockley–Queisser limit in stable, dopant-free triple cation perovskite solar cells, *Energy Environ. Sci.*, 2017, **10**, 1530–1539.
38 S. N. Habisreutinger, *et al.*, Enhanced Hole Extraction in Perovskite Solar Cells Through Carbon Nanotubes, *J. Phys. Chem. Lett.*, 2014, **5**, 4207–4212.
39 E. Aktas, J. Jiménez-López, K. Azizi, T. Torres and E. Palomares, Self-assembled Zn phthalocyanine as a robust p-type selective contact in perovskite solar cells, *Nanoscale Horiz.*, 2020, **5**, 1415–1419.
40 Y. Lin, *et al.*, Self-Assembled Monolayer Enables Hole Transport Layer-Free Organic Solar Cells with 18% Efficiency and Improved Operational Stability, *ACS Energy Lett.*, 2020, **5**, 2935–2944.
41 A. Magomedov, *et al.*, Self-Assembled Hole Transporting Monolayer for Highly Efficient Perovskite Solar Cells, *Adv. Energy Mater.*, 2018, **8**, 1801892.
42 S. N. Habisreutinger, N. K. Noel and H. J. Snaith, Hysteresis Index: A Figure without Merit for Quantifying Hysteresis in Perovskite Solar Cells, *ACS Energy Lett.*, 2018, **3**, 2472–2476.
43 H. J. Snaith, *et al.*, Anomalous hysteresis in perovskite solar cells, *J. Phys. Chem. Lett.*, 2014, **5**, 1511–1515.
44 L. Wang, C. McCleese, A. Kovalsky, Y. Zhao and C. Burda, Femtosecond time-resolved transient absorption spectroscopy of $CH_3NH_3PbI_3$ perovskite films: Evidence for passivation effect of pbi2, *J. Am. Chem. Soc.*, 2014, **136**, 12205–12208.
45 National Renewable Energy Laboratory. PV Efficiency Chart. (2020).
46 Q. Wang, N. Phung, D. Di Girolamo, P. Vivo and A. Abate, Enhancement in lifespan of halide perovskite solar cells, *Energy Environ. Sci.*, 2019, **12**, 865–886.
47 Z. Li, *et al.*, Side-Chain Engineering for Enhancing the Thermal Stability of Polymer Solar Cells, *Adv. Mater.*, 2015, **27**, 6999–7003.
48 M. Petrović, *et al.*, Limitations of a polymer-based hole transporting layer for application in planar inverted perovskite solar cells, *Nanoscale Adv.*, 2019, **1**, 3107–3118.
49 P. Gijsman, G. Meijers and G. Vitarelli, Comparison of the UV-degradation chemistry of polypropylene, polyethylene, polyamide 6 and polybutylene terephthalate, *Polym. Degrad. Stab.*, 1999, **65**, 433–441.
50 M. Stolterfoht, *et al.*, Approaching the fill factor Shockley–Queisser limit in stable, dopant-free triple cation perovskite solar cells, *Energy Environ. Sci.*, 2017, **10**, 1530–1539.
51 M. Saliba, *et al.*, Incorporation of rubidium cations into perovskite solar cells improves photovoltaic performance, *Science*, 2016, **354**, 206–209.
52 A. Farooq, *et al.*, Spectral Dependence of Degradation under Ultraviolet Light in Perovskite Solar Cells, *ACS Appl. Mater. Interfaces*, 2018, **10**, 21985–21990.
53 W. Li, *et al.*, Enhanced UV-light stability of planar heterojunction perovskite solar cells with caesium bromide interface modification, *Energy Environ. Sci.*, 2016, **9**, 490–498.

